Nano Research

Open Access

Research Article

Insight into the metal-free electrocatalysis of heteroatom-doped carbon nanocages in competitive CO_2 reduction and H_2 evolution

Liu Jiao[1], Chenghui Mao[1], Biao Feng[1], Fengfei Xu[1], Shuo Li[2], Jun Zhong[2], Mingqi Xia[1], Ruonan Cui[1], Xizhang Wang[1], Lijun Yang[1]✉, Qiang Wu[1]✉, and Zheng Hu[1]✉

[1] *Key Laboratory of Mesoscopic Chemistry of Ministry of Education (MOE) and Jiangsu Provincial Laboratory for Nanotechnology, School of Chemistry and Chemical Engineering, Nanjing University, Nanjing 210023, China*

[2] *Institute of Functional Nano and Soft Materials Laboratory (FUNSOM), Jiangsu Key Laboratory of Advanced Negative Carbon Technologies, Soochow University, Suzhou 215123, China*

Cite this article: *Nano Research*, **2025**, *18*, 94907171. https://doi.org/10.26599/NR.2025.94907171

ABSTRACT: Metal-free carbon-based catalysts exhibit diverse electrocatalytic performances in CO_2 reduction reaction (CO_2RR), but the attributions and contributions of active sites are still confusing to date. Herein, the hierarchical carbon nanocages (hCNC) doped with different heteroatoms (B, N, P, S) are prepared to examine the impact of dopants on the competitive CO_2RR and hydrogen evolution reaction (HER). The hCNC and P-doped hCNC show little CO_2RR activity, B- and S-doped hCNC show weak CO_2RR activity, while N-doped hCNC presents high CO_2RR activity. The CO Faradaic efficiency (FE_{CO}) of N-containing hCNC increases almost linearly with increasing the N content, even with the co-existing B or P. S- and SN-doped hCNC more facilitate the HER. 16 doping configurations are constructed, and up to 53 sites are examined for the electrochemical activities with a constant potential modelling method. The pyridinic-N(N*) is the best active site for CO_2RR to CO, while CBO_2H_2-1(αC*), CBO_2H_2-2(γC*), NO-1(βC*), PO_2H-3(αC*) and SO_3H-3(δC*) are active for HER. The optimized FE_{CO} achieves 83.6% for N-doped hCNC with 9.54 at.% nitrogen, and S-doped hCNC reaches ca. 30 mA·cm^{-2} current density for HER. This study unveils the structure-performance correlation of heteroatom-doped hCNC, which is conducive to the rational design of advanced metal-free carbon-based catalysts.

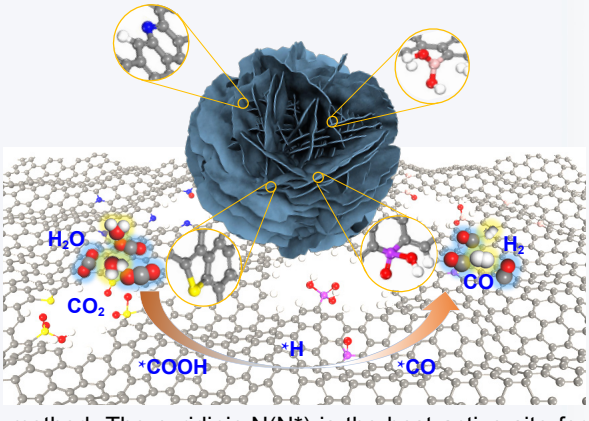

KEYWORDS: heteroatom-doping, metal-free carbon-based catalyst, CO_2 reduction reaction, hydrogen evolution reaction, active sites, density functional theory (DFT)

1 Introduction

Since the discovery of high activity of N-doped carbon nanotube arrays towards oxygen reduction reaction (ORR) [1], carbon-based metal-free catalysts have attracted wide interest in various electrochemical reactions such as hydrogen evolution reaction (HER), oxygen evolution reaction (OER) and carbon dioxide reduction reaction (CO_2RR) [2–6]. The carbons doped with different heteroatoms break the charge neutrality of sp^2 carbons and induce charge redistribution, which can regulate the adsorption/desorption of reaction species, providing the opportunity for improving the electrochemical performance [1, 5, 6]. Although many metal-based catalysts with considerable CO_2RR performances have been reported in recent years [7–9], carbon-based metal-free catalysts have their own advantages such as low cost and abundant resources. Since the first report of CO_2RR with N-doped carbon nanofiber in 2013 [10], various N-doped and co-doped carbons have been developed, which demonstrated excellent performance with CO Faradaic efficiency (FE_{CO}) close to 100% and current density up to 100 mA·cm^{-2} [11–14]. Despite the great progress, there exist many controversial results in CO_2RR of metal-free heteroatom-doped carbon catalysts. For example, for the P- or B-doped carbon, either a high FE_{CO} over 80% [15, 16] or a negligible FE_{CO} while dominant HER activity was reported [13, 17]. The S-doped carbon presented a FE_{CO} of 45% [18] or a negligible FE_{CO} with a strong HER preference [19]. It is seen that the metal-free catalysts showed very different performances even with the

Received: October 2, 2024; **Revised:** November 18, 2024
Accepted: December 4, 2024

✉Address correspondence to Lijun Yang, lijunyang@nju.edu.cn; Qiang Wu, wqchem@nju.edu.cn; Zheng Hu, zhenghu@nju.edu.cn

same heteroatom dopants. Moreover, the attributions of active sites are also confusing, with different claims of pyridinic-N (Py-N) [20], quaternary N (G-N) [21], pyrrolic-N (Pr-N) [12, 22], and the adjacent C of N dopants [10, 23] as the dominant active sites for CO_2RR. This situation indicates the complexity of this topic, due to the many differences in, e.g., pore structure, specific surface areas (SSA), and conductivity of the carbon matrix [24]. Hence, to better understand the impact of different heteroatom dopants on CO_2RR activity, the use of nanocarbons with the similar architecture should be recommended.

Hierarchical carbon nanocages (hCNC) developed by our group have large specific surface area, micro-meso-macropores, and high conductivity, which can facilitate the synergic mass/charge transfer and active sites accessibility [25–27]. Moreover, hCNC can be easily doped with different heteroatoms without compromising its original architecture, providing a good platform for the study of metal-free electrocatalysis [28, 29]. Herein, we introduced four kinds of heteroatoms (B, N, P, S) into hCNC to explore the correlation between heteroatom dopants and activity/selectivity of the competitive CO_2RR and HER. We have conducted a more comprehensive investigation on possible active sites of heteroatom dopants. It is found that, hCNC and P-doped hCNC show little CO_2RR activity, B- and S-doped hCNC show weak CO_2RR activity, while N-doped hCNC presents much improved CO_2RR activity. The FE_{CO} of N-doped hCNC increases almost linearly with increasing N content, even in the presence of B or P, while the S- and SN-doped hCNC more facilitate the HER. The theoretical calculations reveal that the pyridinic-N(N*) is the most favorable active site for CO_2RR to CO, while CBO_2H_2-1(αC*), CBO_2H_2-2(γC*), NO-1(βC*), PO_2H-3(αC*) and SO_3H-3(δC*) are active to HER. The N-hCNC with N content of 9.54 at.% reaches a FE_{CO} of 83.6% at −0.5 V, and S-hCNC exhibits the maximum HER current density approaching 30 $mA·cm^{-2}$ at −1.0 V. The experimental results and theoretical understanding in this study are significant for the rational design of advanced metal-free carbon-based catalysts for CO_2RR.

2 Experimental

2.1 Catalyst preparation

The hierarchical carbon-based nanocages were used as metal-free catalysts, which were prepared by the *in situ* MgO template method at 800 °C [25, 28, 29]. The pure (undoped) and heteroatom-doped hierarchical carbon nanocages were obtained with benzene, phenylboronic acid, pyridine, triphenylphosphine, and thiophene precursors, denoted as hCNC and X-hCNC (X = B, N, P, S), respectively (Scheme S1 in the Electronic Supplementary Material (ESM)). For preparing the co-doped hCNC, the mixed organic precursors were used.

2.2 Theoretical calculations

All the spin-unrestricted density functional theory (DFT) calculations were performed with the package of DMol³ 8.0 [30, 31]. The constant potential modelling method was used to simulate the CO_2RR and HER processes at −0.6 V to make the modeling condition closer to the actual reaction environment [32].

2.3 Electrochemical tests

The CO_2RR performance was evaluated in an H-type electrochemical cell with two compartments separated by a Nafion®117 proton exchange membrane. Ag/AgCl electrode (3.0 $mol·L^{-1}$ KCl) and Pt wire were used as the reference and counter electrodes, respectively. All potentials were referenced to a reversible hydrogen electrode (RHE) with the following equation, $E_{RHE} = E_{Ag/AgCl} + 0.209 + 0.0592 \times pH$, where E_{RHE} is the potential vs. RHE and $E_{Ag/AgCl}$ is the measured potential vs. Ag/AgCl electrode. The electrolyte was CO_2-saturated 0.5 $mol·L^{-1}$ $KHCO_3$ solution. The high-purity CO_2 gas (99.99%) was bubbled into the cathodic electrolyte with a flow rate of 20 $mL·min^{-1}$. The linear sweep voltammetry (LSV) curve was performed under the range of 0–−1.0 V with a scan rate of 1 $mV·s^{-1}$. The CO_2RR chronoamperometric (CP) test was conducted at each potential (−0.5–−1.0 V with 0.1 V intervals) for 720 s, and the resulting gaseous products were analyzed by on-line gas chromatography (GC, hope-9860-5CNJ) to calculate the FE and partial current density (j) of CO and H_2. More details about experiment and theoretical calculation can be found in the ESM.

3 Results and discussion

Figure 1 provides the typical scanning electron microscopy (SEM) and transmission electron microscopy (TEM) images of hCNC and X-hCNC (X = B, N, P, S). The as-prepared hCNC shows a

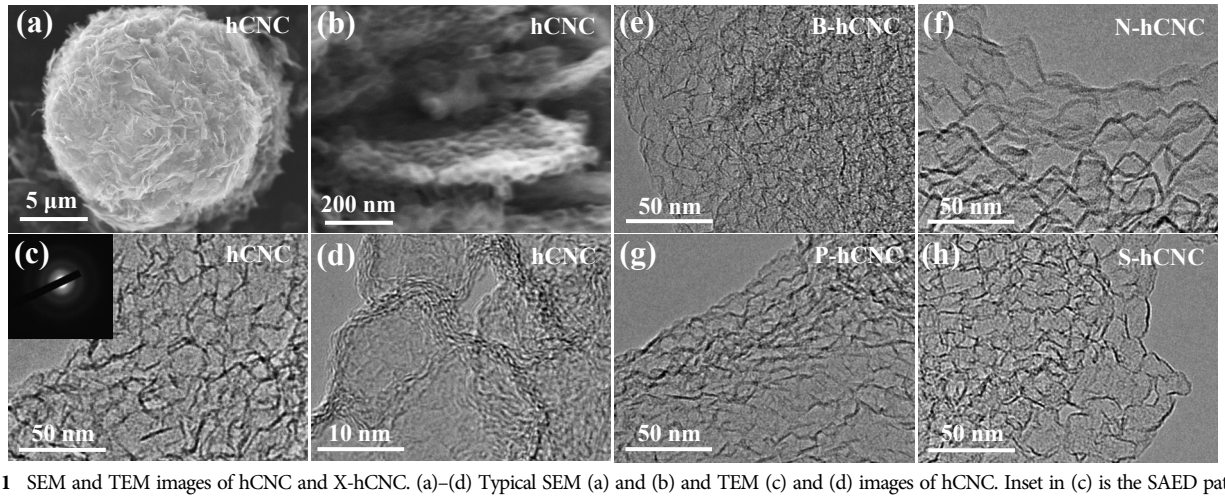

Figure 1 SEM and TEM images of hCNC and X-hCNC. (a)–(d) Typical SEM (a) and (b) and TEM (c) and (d) images of hCNC. Inset in (c) is the SAED pattern of hCNC. (e)–(h) TEM images of B-hCNC (e), N-hCNC (f), P-hCNC (g), and S-hCNC (h).

morphology of porous micron-sized spheric particles composed of nanosheets (Fig. 1(a)). The nanosheets have submicron-sized interspace and consist of interconnected hollow nanocages of 10–30 nm in size (Figs. 1(b)–1(d)). The selected-area electron diffraction (SAED) pattern of the hCNC only shows dispersion halos, indicating the relatively low crystallinity of carbon shell and the absence of any residual MgO template (Fig. 1(c)). The heteroatom-doped hCNC remain the hierarchical structure with high structural similarity (Figs. 1(e)–1(h)). The high-angle annular dark-field scanning TEM (HAADF-STEM) element mapping images revealed the high distribution of B, N, P, and S species in the corresponding X-hCNC (Fig. S1 in the ESM). hCNC and X-hCNC have comparable high SSA (> 1300 $m^2 \cdot g^{-1}$) and hierarchical pore structure with coexisting micro-meso-macropores (Fig. S2 in the ESM), which could facilitate the electrolyte accessibility of active sites and synergic mass/charge transfer [33, 34]. All the samples have good graphitization degree and high bulk conductivity, with similar I_D/I_G (intensity ratio of D to G mode) values in Raman spectra (Fig. S3 in the ESM).

Multiple spectroscopic characterizations were conducted to probe the bonding configurations of heteroatoms, as shown in Fig. 2. X-ray photoelectron spectroscopy (XPS) results indicate that four types of heteroatoms (B, N, P, S) are successfully doped into carbon nanocages (Table S1 in the ESM). Deconvolution of XPS signals were performed with reference to the reported heteroatom-doped carbon-based materials [16, 35–40]. No residual Mg species were detected in these hCNC samples, again indicating the complete removal of MgO template by acid etching (Fig. S4 in the ESM) [41, 42]. Specifically, undoped hCNC has typical sp^2-hybridized carbon (284.8 eV) and a few O-containing species (286.3 eV for C–O, 2869.9 eV for C=O, 289.1 eV for O–C=O) and π–π* (291.0 eV) (Fig. 2(a)) [35, 36], and the C–X bonds appear in the C 1s spectra of corresponding X-hCNC (Fig. S5 in the ESM) [16, 37, 38]. B-hCNC has edge C_2BO (192.3 eV) and CBO_2 (190.9 eV) species (Fig. 2(b)) [36, 39]. N-hCNC has four N species, i.e., graphitic-N (401.1 eV), edge pyridinic-N (398.3 eV), edge pyrrolic-N (399.4 eV) and oxidized N (404.5 eV) (Fig. 2(c)) [37, 38]. P-hCNC probably has P–C (131.8/132.7 eV) and P–O (133.0/133.9 eV) species (Fig. 2(d)) [40]. S-hCNC has edge C–S–C (164.0/165.2 eV) and SO_x species (168.5/169.7 eV) (Fig. 2(e)) [37].

The consistent results are demonstrated by soft X-ray absorption spectroscopy (XAS) analysis (Fig. 2 and Fig. S6 in the ESM). In the C K-edge spectrum, the resonance peaks at 285.4 and 292.4 eV are attributed to the unoccupied C=C π* and C=C σ*, which represent graphite-like structure (Fig. 2(f)) [43, 44]. Additional signals between the π* and σ* peaks can be ascribed to the fingerprints of hCNC and X-hCNC. Both hCNC and X-hCNC have a peak at 288.4 eV, which stems from different C–C bond lengths at the edges of graphite layer, usually attaching the carboxyl (–COOH) groups [45, 46]. All the X-hCNC samples exhibit a new peak at 287.0 eV compared with hCNC, indicating the existence of C–X bonds [27, 47–49]. In the corresponding XAS spectra, the B K-edge of B-hCNC has weak intensities for C_2BO and CBO_2 signals due to the low B content (Fig. S6(a) in the ESM) [50]; the N K-edge of N-hCNC features the main signals of pyridinic-N and graphitic-N (Fig. S6(b) in the ESM) [48–50]; the P L-edge of P-hCNC exhibits the signals of P–C and multiple P–O groups (Fig. S6(c) in the ESM) [51–53]; the S L-edge of S-hCNC exhibits the signals of thiophene S and S–O groups (Fig. S6(d) in the ESM) [54].

The electrochemical CO_2RR performances of these carbon-based metal-free catalysts were evaluated in 0.5 M $KHCO_3$ aqueous electrolyte, as shown in Fig. 3 (Figs. S7–S13 in the ESM). The LSV curves tested in CO_2 or Ar atmosphere indicate the sole HER activities of hCNC and P-hCNC, high CO_2RR activity of N-hCNC, and dominant HER activities of B-hCNC and S-hCNC with weak CO_2RR activities at low potentials (Fig. S7 in the ESM). The gas products were analyzed by online GC after the CO_2RR at a fixed potential (−0.5–−1.0 V) for 720 s, which are composed of CO and H_2 and no liquid products were detected in the electrolytes by ^{1}H-nuclear magnetic resonance (^{1}H NMR) (Fig. 3(a) and Fig. S8 in the

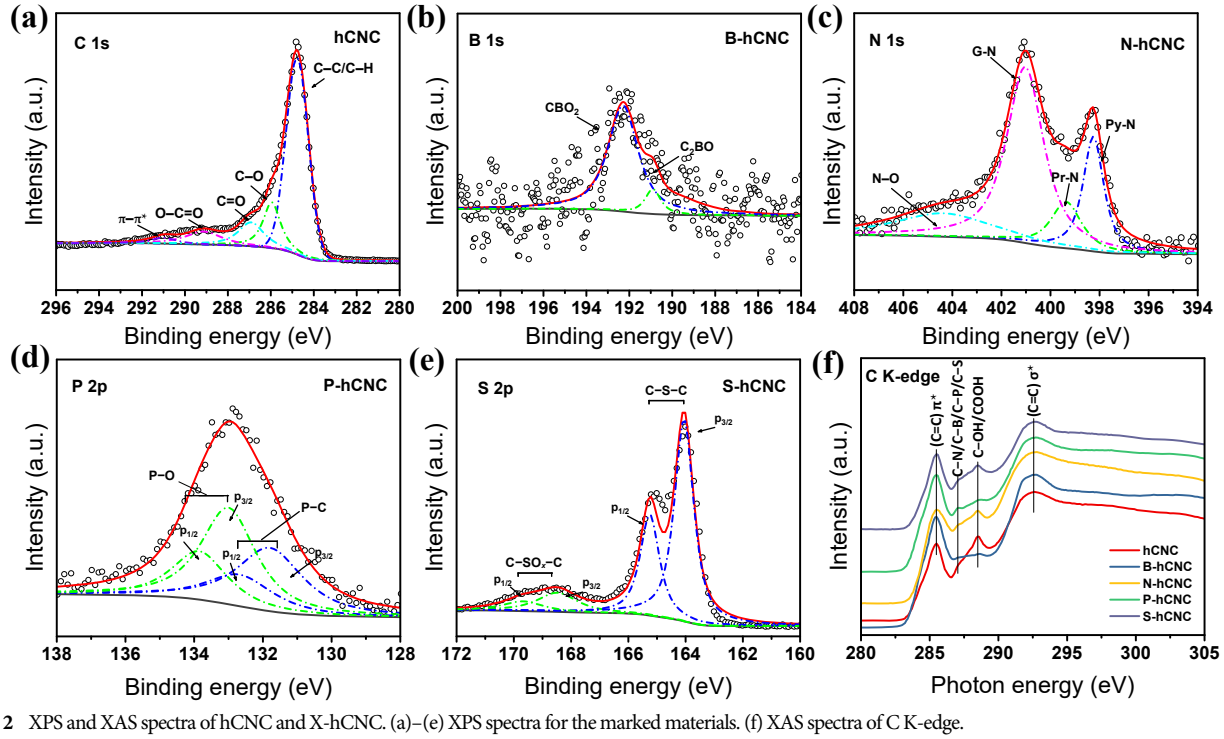

Figure 2 XPS and XAS spectra of hCNC and X-hCNC. (a)–(e) XPS spectra for the marked materials. (f) XAS spectra of C K-edge.

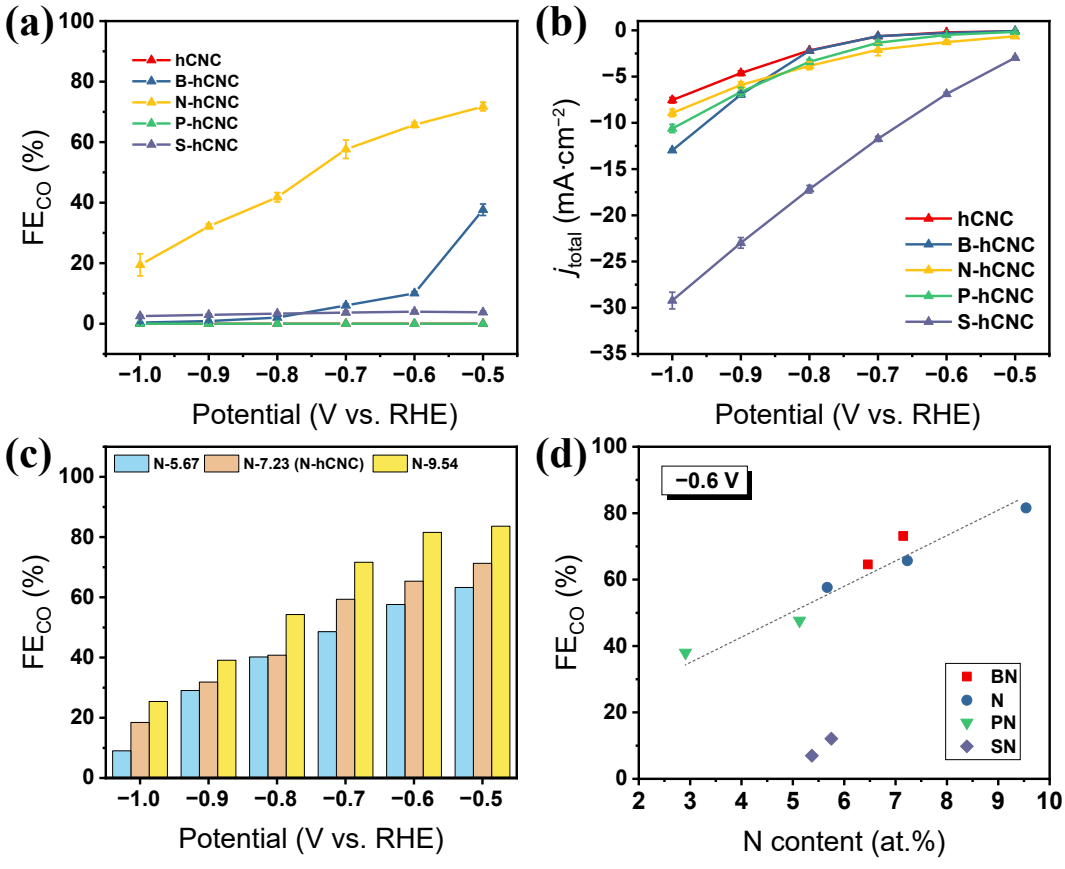

Figure 3 CO_2RR performances of hCNC, X-hCNC and XN-hCNC. (a) FE_{CO} of hCNC and X-hCNC. (b) j_{total} of hCNC and X-hCNC. (c) FE_{CO} of N-hCNC with different N contents. (d) The relationship between FE_{CO} and N contents of XN-hCNC at −0.6 V. Note: The error bar is obtained based on the results of three experiments.

ESM). Specifically, hCNC and P-hCNC only produce H_2, but B-hCNC, N-hCNC and S-hCNC produce both CO and H_2. Compared with hCNC, P-hCNC has higher H_2 partial current density (j_{H2}) (Figs. S9(a)–S9(c) in the ESM). The FE_{CO} of N-hCNC is 71.3% at −0.5 V and decreases gradually to ~ 20% at −1.0 V. The FE_{CO} of B-hCNC is about 40% at −0.5 V and decays quickly to below 5% with increasing the potential (Fig. 3(a)), and the CO partial current density (j_{CO}) is always below 1 mA·cm^{-2} in the range of −0.5–−1.0 V (Fig. S9(a) in the ESM). In contrast, the j_{CO} of N-hCNC is always larger than those of other samples, with the highest value of 1.9 mA·cm^{-2} at −0.9 V (Fig. S9(a) in the ESM). S-hCNC has much better HER activity than that of CO_2RR, with a negligible j_{CO} (< 0.8 mA·cm^{-2}) and a high j_{H2} of nearly 30 mA·cm^{-2} at −1.0 V (Figs. S9(a) and S9(b) in the ESM). In addition, the hCNC and X-hCNC showed decent stabilities in 10 h electrochemical tests and kept good structure (Figs. S10 and S11 in the ESM). The above results show that the heteroatom doping can increase the response current of hCNC to some extent, with the highest total current density (j_{total}) for S-hCNC (Fig. 3(b)). S-hCNC has the smallest charge transfer resistance (R_{ct}), corresponding to its highest j_{total} (Fig. S12 in the ESM). N-hCNC has the largest electrochemical active surface area (ECSA)-normalized j_{CO} and S-hCNC has the largest ECSA-normalized j_{H2}. B, N, P and S doping enhance the HER or CO_2RR current densities (Fig. S13 in the ESM). The CO_2 adsorption capacities of hCNC and X-hCNC were also taken into consideration (Fig. S14 in the ESM). The CO_2 adsorption tests showed that hCNC, B-hCNC, and N-hCNC have close CO_2 adsorption capacities, which are higher than that of S-hCNC and P-hCNC. The lower CO_2 adsorption volume may potentially account for the inferior CO_2RR performance of S-hCNC and P-hCNC. According to the preceding results, hCNC and X-hCNC have high SSA, high conductivity, high CO_2 adsorption capacity, and a variety of different doping configurations in the carbon skeleton, which provide a good platform to investigate the correlation between heteroatom dopants and activity/selectivity of the competitive CO_2RR and HER.

Considering the good CO_2RR-to-CO performance of N-hCNC, the influence of N content was further investigated (Fig. 3(c), Figs. S15 and S16 in the ESM). It is found that the FE_{CO} at fixed potentials increases gradually with increasing the N content from 5.67 at.% via 7.23 at.% to 9.54 at.% (Fig. 3(c) and Table S2 in the ESM). A series of N and X co-doped XN-hCNC (X = B, P, S) catalysts were synthesized to probe the influence of dopants on the product selectivity, and FE_{CO} increases almost linearly with the N content (ranges from 3 at.% to 10 at.%) at each potential, even with the co-doped P and B heteroatoms (Fig. 3(d), Table S2 and Figs. S17–S20 in the ESM). This result further demonstrates the decisive role of N dopants in the CO_2RR to CO. For the SN-hCNC, the FE_{CO} is far below the linear range, which could be ascribed to the strong activity of S dopants towards HER to inhibit the CO_2RR on neighboring N dopants. Additionally, the CO_2RR performance of N-hCNC can be optimized by heating at higher temperatures, with the highest FE_{CO} of 92.5% at −0.5 V, which is close to the literature level [4, 11, 12, 23, 24, 55, 56]. In summary, there is a positive correlation between CO_2RR to CO activity and N content, while B, P, and S doping increase the current density of HER, which implies the distinct roles of different heteroatom dopants in the competitive CO_2RR and HER. The results fill the gap in understanding the role

of non-N heteroatom dopants in CO_2RR, enabling a direct comparison on the same platform (Tables S3 and S4 in the ESM).

The active structures in these carbon-based catalysts and corresponding electrocatalytic selectivity towards CO_2RR and HER were screened and simulated by DFT calculations, as shown in Fig. 4. Firstly, 16 dopant models including intrinsic C sites were constructed at the edge of the micropores based on the XPS and XAS results (Figs. 4(a) and 4(b) and Figs. S21 and S22 in the ESM). The C atoms near the heteroatoms were also included in the screening of active sites, and the first, second, third and fourth C atoms adjacent to the heteroatoms are referred to as αC, βC, γC and δC, respectively. In total, 53 sites were investigated to screen out the possible CO_2RR active sites. Among them, 23 sites can adsorb CO_2, and the CO_2RR and HER reaction process on these sites was calculated by the constant potential modelling method at −0.6 V (Fig. S21(a) in the ESM, green circle) [32]. In strict adherence to Sabatier principle, an adsorption energy reference of ± 0.50 eV was established to ensure the optimal $*CO_2$/*H adsorption [57], and 14 sites were screened out based on this principle (blue box in Fig. S21(b) in the ESM). Both B and P dopants have only 1 preferential structure (CBO_2H_2 and PO_2H), while N and S dopants have 3 preferential dopant structures (N: G-N, Py-N, NO; S: Thio-S, Thio-SO_2, SO_3H) (Fig. 4(c)). Most of these sites enhance both CO_2RR and HER as described in the lower-left quadrant of Fig. 4(c).

To further examine how heteroatoms affect the competition between CO_2RR and HER on a site, $\Delta G_{rds\text{-}CO_2RR} - \Delta G_{rds\text{-}HER}$ is selected as the descriptor, which is the difference between the Gibbs free energy change of the rate-determining step for CO_2RR ($\Delta G_{rds\text{-}CO_2RR}$) and HER ($\Delta G_{rds\text{-}HER}$) (Fig. 4(d)). We choose the value of pristine carbon (hole–C*) as the origin point, and the heteroatom doping may shift this value and thus change the thermodynamic preference between CO_2RR and HER with respect to pristine carbon. Specifically, the CO_2RR preference of carbon-based catalysts can be enhanced by the doping sites of CBO_2H_2-3(δC*), Py-N-1(N*), Py-N-2(βC*), G-N-3(βC*), NO-3(γC*), PO_2H-4(γC*), Thio-S-1(γC*) and SO_2-2(γC*). Among them, Py-N-1(N*), G-N-3(βC*), CBO_2H_2-3(δC*) and SO_2-2(γC*) have a significant reduction in $\Delta G_{rds\text{-}CO_2RR} - \Delta G_{rds\text{-}HER}$, with the most significant reduction for Py-N-1(N*). The HER activity of carbon-based catalysts can be enhanced by the doping sites of CBO_2H_2-1(αC*), CBO_2H_2-2(γC*), NO-1(βC*), PO_2H-3(αC*) and SO_3H-3(δC*).

Combing the theoretical and experimental results (Table 1), it is learnt that most of the N species favor CO_2RR over HER, with the best active site of Py-N-1(N*) for CO_2RR, endowing N-hCNC with the highest FE_{CO} and j_{CO}. For B-hCNC, CBO_2H_2-3(δC*) sites favor CO_2RR, whereas CBO_2H_2-1(αC*) and CBO_2H_2-2(γC*) strongly favor HER. The low B doping amount limits its performance. For P-hCNC, the PO_2H-4(γC*) favors CO_2RR very slightly, but the PO_2H-3(αC*) strongly favors HER, hence showing the dominant HER. For S-hCNC, the main S-doping site of SO_3H-3(δC*) has a strong enhancement effect on HER, leading to a larger HER current

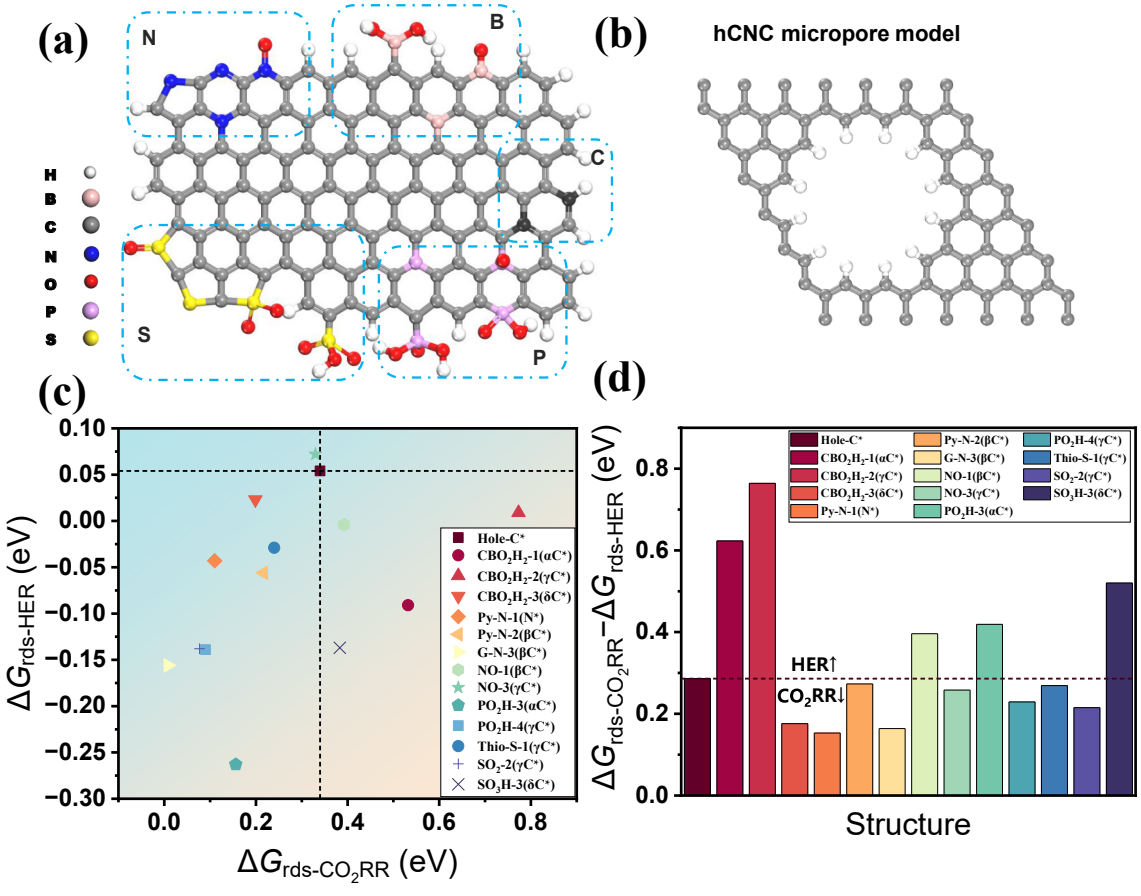

Figure 4 Heteroatom-doping models and the comparison of reaction Gibbs free energies. (a) Heteroatom-doping models. (b) Modeling crystal cell diagram of micropore. (c) The Gibbs free energy change of the rate-determing step (ΔG_{rds}) comparison of CO_2RR and HER. (d) The difference in ΔG_{rds} between CO_2RR and HER. Black/grey, pink, blue, red, yellow, purple, and white represent C, B, N, O, S, P, and H atoms, respectively. The dashed line corresponds to the ($\Delta G_{rds\text{-}CO_2RR} - \Delta G_{rds\text{-}HER}$) for intrinsic C* site.

Table 1 Summary of heteroatom-doped active sites for CO_2RR and HER[a]

Element	Configuration	CO_2RR sites	HER sites	Apparent performance
B	CBO_2H_2	δC*	αC*, γC*	HER
N	Py-N, G-N, NO	Py-N: N*, βC*; G-N: βC*; NO: γC*	NO: γC*	Strong CO_2RR
P	PO_2H	γC*	αC*	HER
S	Thio-S, SO_2, SO_3H	Thio-S: γC*; SO_2: γC*	SO_3H: δC*	Strong HER

[a]The site Py-N: N* represents the main active site for CO_2RR, and the sites B: αC*, γC*; P: αC*; SO_3H: δC* represent the main active sites for HER.

density. When improving the annealing temperature to 1000 °C, the proportion of SO_x species decrease and the proportion of C–S–C species increase, the SN-hCNC can achieve a higher FE_{CO} of 91.2% at −0.6 V (Fig. S23 in the ESM). The theoretical results are consistent with the observed electrochemical performances of hCNC and X-hCNC (Fig. 3(a)).

4 Conclusions

Heteroatom (B, N, P, S) mono-doped/co-doped carbon nanocages were prepared to examine the dopants' impact on the competitive CO_2RR and HER by combined experimental and theoretical studies. The results indicate that undoped hCNC and P-hCNC have little CO_2RR activity, B-hCNC and S-hCNC show weak CO_2RR activity, while N-hCNC presents improved CO_2RR activity. The FE_{CO} of N-doped carbons increases almost linearly with increasing the N content, even in the presence of B or P atoms, while the S-hCNC more facilitates the HER. The theoretical calculations reveal that the Py-N-1(N*) is the most favorable active site for CO_2RR to CO, while CBO_2H_2-1(αC*), CBO_2H_2-2(γC*), PO_2H-3(αC*) and SO_3H-3(δC*) are active to HER. The low B and P doping amounts hinder the CO_2RR partial current densities of B-hCNC and P-hCNC, and S-hCNC shows the largest current density due to the strong HER of the SO_3H-3(δC*) site and high S content. The results of this study deepen the understanding of the relationship between active sites and catalytic performance, thereby aiding in the design of efficient metal-free carbon-based catalysts for CO_2RR.

Electronic Supplementary Material: Supplementary material (further details of synthesis procedures; SEM, TEM, element mapping, Brunauer–Emmett–Teller (BET), XPS, XAS, X-ray diffraction (XRD), Raman spectroscopy and NMR measurements; electrochemical experiments and calculation details) is available in the online version of this article at https://doi.org/10.26599/NR.2025.94907171.

Data availability

All data needed to support the conclusions in the paper are presented in the manuscript and the Electronic Supplementary Material. Additional data related to this paper may be requested from the corresponding author upon request.

Acknowledgements

This work was jointly supported by the National Key Research and Development Program of China (No. 2021YFA1500900), the National Natural Science Foundation of China (No. 52071174), and the Natural Science Foundation of Jiangsu Province, Major Project (No. BK20212005). The numerical calculations have been done on the computing facilities in the High Performance Computing Center (HPCC) of Nanjing University. We thank the staff at Hefei Synchrotron Radiation Facility (MCD-A and MCD-B Soochow Beamline for Energy Materials at NSRL).

Declaration of competing interest

All the contributing authors report no conflict of interests in this work.

Author contribution statement

L. J.: Investigation, methodology, writing – original draft. C. H. M.: Methodology, software. B. F.: Methodology, validation. F. F. X.: Validation. S. L.: Formal analysis. J. Z.: Resources. M. Q. X.: Methodology. R. N. C.: Investigation. X. Z. W.: Formal analysis, methodology. L. J. Y.: Methodology, software, validation. Q. W.: Conceptualization, supervision, writing – review & editing. Z. H.: Supervision, funding acquisition, writing – review & editing. All the authors have approved the final manuscript.

Use of AI statement

None.

References

[1] Gong, K. P.; Du, F.; Xia, Z. H.; Durstock, M.; Dai, L. M. Nitrogen-doped carbon nanotube arrays with high electrocatalytic activity for oxygen reduction. *Science* **2009**, *323*, 760–764.
[2] Hu, C. G.; Paul, R.; Dai, Q. B.; Dai, L. M. Carbon-based metal-free electrocatalysts: From oxygen reduction to multifunctional electrocatalysis. *Chem. Soc. Rev.* **2021**, *50*, 11785–11843.
[3] Yang, L. J.; Shui, J. L.; Du, L.; Shao, Y. Y.; Liu, J.; Dai, L. M.; Hu, Z. Carbon-based metal-free ORR electrocatalysts for fuel cells: Past, present, and future. *Adv. Mater.* **2019**, *31*, 1804799.
[4] Duan, X. C.; Xu, J. T.; Wei, Z. X.; Ma, J. M.; Guo, S. J.; Wang, S. Y.; Liu, H. K.; Dou, S. X. Metal-free carbon materials for CO_2 electrochemical reduction. *Adv. Mater.* **2017**, *29*, 1701784.
[5] Wang, B.; Liu, B. W.; Dai, L. M. Non-N-doped carbons as metal-free electrocatalysts. *Adv. Sustain. Syst.* **2021**, *5*, 2000134.
[6] Gao, K.; Wang, B.; Tao, L.; Cunning, B. V.; Zhang, Z. P.; Wang, S. Y.; Ruoff, R. S.; Qu, L. T. Efficient metal-free electrocatalysts from N-doped carbon nanomaterials: Mono-doping and co-doping. *Adv. Mater.* **2019**, *31*, 1805121.
[7] Ding, J. Y.; Wei, T. R.; Hou, T.; Liu, W. J.; Liu, Q.; Zhang, H.; Luo, J.; Liu, X. J. Easily constructed porous silver films for efficient catalytic CO_2 reduction and Zn–CO_2 batteries. *Nanoscale* **2024**, *16*, 10628–10636.
[8] Meng, Y. C.; Ding, J. Y.; Liu, Y. F.; Hu, G. Z.; Feng, Y. H.; Wu, Y. H.; Liu, X. J. Advancements in amorphous oxides for electrocatalytic carbon dioxide reduction. *Mater. Today Catal.* **2024**, *7*, 100065.
[9] Wei, T. R.; Zhang, S. S.; Liu, Q.; Qiu, Y.; Luo, J.; Liu, X. J. Oxygen

vacancy-rich amorphous copper oxide enables highly selective electroreduction of carbon dioxide to ethylene. *Acta Phys. Chim. Sin.* **2023**, *39*, 2207026.

[10] Kumar, B.; Asadi, M.; Pisasale, D.; Sinha-Ray, S.; Rosen, B. A.; Haasch, R.; Abiade, J.; Yarin, A. L.; Salehi-Khojin, A. Renewable and metal-free carbon nanofibre catalysts for carbon dioxide reduction. *Nat. Commun.* **2013**, *4*, 2819.

[11] Fernandes, D. M.; Peixoto, A. F.; Freire, C. Nitrogen-doped metal-free carbon catalysts for (electro)chemical CO_2 conversion and valorisation. *Dalton Trans.* **2019**, *48*, 13508–13528.

[12] Sun, G. D.; Cao, Y. N.; Hu, M. Z.; Liang, X. H.; Wang, Z.; Cai, Z. J.; Shen, F. Y.; He, H.; Wang, Z. X.; Zhou, K. B. Pyrrolic N-doped carbon catalysts for highly efficient electrocatalytic reduction of CO_2 with superior CO selectivity over a wide potential window. *Carbon* **2023**, *214*, 118320.

[13] Zheng, W. Z.; Wang, D. S.; Zhang, Y. K.; Zheng, S. X.; Yang, B.; Li, Z. J.; Rodriguez, R. D.; Zhang, T.; Lei, L. C.; Yao, S. Y. et al. Promoting industrial-level CO_2 electroreduction kinetics via accelerating proton feeding on a metal-free aerogel electrocatalyst. *Nano Energy* **2023**, *105*, 107980.

[14] Yang, H. P.; Wu, Y.; Lin, Q.; Fan, L. D.; Chai, X. Y.; Zhang, Q. L.; Liu, J. H.; He, C. X.; Lin, Z. Q. Composition tailoring via N and S co-doping and structure tuning by constructing hierarchical pores: Metal-free catalysts for high-performance electrochemical reduction of CO_2. *Angew. Chem., Int. Ed.* **2018**, *57*, 15476–15480.

[15] Xie, J. F.; Ghausi, M. A.; Wang, J.; Wang, X. Y.; Wang, W.; Yang, R.; Wu, M. X.; Zhang, Q. B.; Wang, Y. B. Low-energy CO_2 reduction on a metal-free carbon material. *ChemElectroChem* **2020**, *7*, 2145–2150.

[16] Cheng, C. F.; Shao, J. Q.; Wei, P. F.; Song, Y. P.; Li, H. F.; Gao, D. F.; Wang, G. X. Nitrogen and boron co-doped carbon spheres for carbon dioxide electroreduction. *ChemNanoMat* **2021**, *7*, 635–640.

[17] Jia, C.; Ren, W. H.; Chen, X. J.; Yang, W. F.; Zhao, C. (N, B) dual heteroatom-doped hierarchical porous carbon framework for efficient electroreduction of carbon dioxide. *ACS Sustain. Chem. Eng.* **2020**, *8*, 6003–6010.

[18] Li, R. R.; Liu, F.; Zhang, Y. H.; Guo, M. M.; Liu, D. Nitrogen, sulfur co-doped hierarchically porous carbon as a metal-free electrocatalyst for oxygen reduction and carbon dioxide reduction reaction. *ACS Appl. Mater. Interfaces* **2020**, *12*, 44578–44587.

[19] Wang, G. X.; Liu, M. Y.; Jia, J. C.; Xu, H. M.; Zhao, B. S.; Lai, K. Y.; Tu, C. Y.; Wen, Z. H. Nitrogen and sulfur co-doped carbon nanosheets for electrochemical reduction of CO_2. *ChemCatChem* **2020**, *12*, 2203–2208.

[20] Liu, S.; Yang, H. B.; Huang, X.; Liu, L. H.; Cai, W. Z.; Gao, J. J.; Li, X. N.; Zhang, T.; Huang, Y. Q.; Liu, B. Identifying active sites of nitrogen-doped carbon materials for the CO_2 reduction reaction. *Adv. Funct. Mater.* **2018**, *28*, 1800499.

[21] Xu, J. Y.; Kan, Y. H.; Huang, R.; Zhang, B. S.; Wang, B. L.; Wu, K. H.; Lin, Y. M.; Sun, X. Y.; Li, Q. F.; Centi, G. et al. Revealing the origin of activity in nitrogen-doped nanocarbons towards electrocatalytic reduction of carbon dioxide. *ChemSusChem* **2016**, *9*, 1085–1089.

[22] Cui, X. Q.; Pan, Z. Y.; Zhang, L. J.; Peng, H. S.; Zheng, G. F. Selective etching of nitrogen-doped carbon by steam for enhanced electrochemical CO_2 reduction. *Adv. Energy Mater.* **2017**, *7*, 1701456.

[23] Li, J. J.; Zan, W. Y.; Kang, H. X.; Dong, Z. P.; Zhang, X. M.; Lin, Y. X.; Mu, Y. W.; Zhang, F. W.; Zhang, X. M.; Gu, J. Graphitic-N highly doped graphene-like carbon: A superior metal-free catalyst for efficient reduction of CO_2. *Appl. Catal. B: Environ.* **2021**, *298*, 120510.

[24] Fu, S. L.; Li, M.; De Jong, W.; Kortlever, R. Tuning the properties of N-doped biochar for selective CO_2 electroreduction to CO. *ACS Catal.* **2023**, *13*, 10309–10323.

[25] Lyu, Z. Y.; Xu, D.; Yang, L. J.; Che, R. C.; Feng, R.; Zhao, J.; Li, Y.; Wu, Q.; Wang, X. Z.; Hu, Z. Hierarchical carbon nanocages confining high-loading sulfur for high-rate lithium-sulfur batteries. *Nano Energy* **2015**, *12*, 657–665.

[26] Wu, Q.; Yang, L. J.; Wang, X. Z.; Hu, Z. Carbon-based nanocages: A new platform for advanced energy storage and conversion. *Adv. Mater.* **2020**, *32*, 1904177.

[27] Wu, Q.; Yang, L. J.; Wang, X. Z.; Hu, Z. Mesostructured carbon-based nanocages: An advanced platform for energy chemistry. *Sci. China Chem.* **2020**, *63*, 665–681.

[28] Zhang, H.; Li, X.; Zhang, D.; Zhang, L.; Kapilashrami, M.; Sun, T.; Glans, P. A.; Zhu, J. F.; Zhong, J.; Hu, Z. et al. Comprehensive electronic structure characterization of pristine and nitrogen/phosphorus doped carbon nanocages. *Carbon* **2016**, *103*, 480–487.

[29] Li, G. C.; Mao, K.; Liu, M.; Yan, M. L.; Zhao, J.; Zeng, Y.; Yang, L. J.; Wu, Q.; Wang, X. Z.; Hu, Z. Achieving ultrahigh volumetric energy storage by compressing nitrogen and sulfur dual-doped carbon nanocages via capillarity. *Adv. Mater.* **2020**, *32*, 2004632.

[30] Delley, B. An all-electron numerical method for solving the local density functional for polyatomic molecules. *J. Chem. Phys.* **1990**, *92*, 508–517.

[31] Delley, B. From molecules to solids with the DMol^3 approach. *J. Chem. Phys.* **2000**, *113*, 7756–7764.

[32] Mao, K.; Yang, L. J.; Wang, X. Z.; Wu, Q.; Hu, Z. Identifying iron-nitrogen/carbon active structures for oxygen reduction reaction under the effect of electrode potential. *J. Phys. Chem. Lett.* **2020**, *11*, 2896–2901.

[33] Chen, Y. Q.; Zhang, J. R.; Tian, J. Y.; Guo, Y.; Xu, F. F.; Zhang, Y.; Wang, X. Z.; Yang, L. J.; Wu, Q.; Hu, Z. Hierarchical Ni/N/C single-site catalyst achieving industrial-level current density and ultra-wide potential plateau of high CO Faradic efficiency for CO_2 electroreduction. *Adv. Funct. Mater.* **2023**, *33*, 2214658.

[34] Jiao, L.; Mao, C. H.; Xu, F. F.; Cheng, X. Y.; Cui, P. X.; Wang, X. Z.; Yang, L. J.; Wu, Q.; Hu, Z. Constructing gold single-atom catalysts on hierarchical nitrogen-doped carbon nanocages for carbon dioxide electroreduction to syngas. *Small* **2024**, *20*, 2305513.

[35] Chen, X. N.; Wang, X. H.; Fang, D. A review on C 1s XPS-spectra for some kinds of carbon materials. *Fullerenes Nanotubes Carbon Nanostruct.* **2020**, *28*, 1048–1058.

[36] Jiao, Y.; Zheng, Y.; Jaroniec, M.; Qiao, S. Z. Origin of the electrocatalytic oxygen reduction activity of graphene-based catalysts: A roadmap to achieve the best performance. *J. Am. Chem. Soc.* **2014**, *136*, 4394–4403.

[37] Yang, F. Q.; Yu, H. M.; Mao, X. Y.; Meng, Q. G.; Chen, S. X.; Deng, Q.; Zeng, Z. L.; Wang, J.; Deng, S. G. Boosting electrochemical CO_2 reduction on ternary heteroatoms-doped porous carbon. *Chem. Eng. J.* **2021**, *425*, 131661.

[38] Yan, D. F.; Dou, S.; Tao, L.; Liu, Z. J.; Liu, Z.; Huo, J.; Wang, S. Y. Electropolymerized supermolecule derived N, P co-doped carbon nanofiber networks as a highly efficient metal-free electrocatalyst for the hydrogen evolution reaction. *J. Mater. Chem. A* **2016**, *4*, 13726–13730.

[39] Sreekanth, N.; Nazrulla, M. A.; Vineesh, T. V.; Sailaja, K.; Phani, K. L. Metal-free boron-doped graphene for selective electroreduction of carbon dioxide to formic acid/formate. *Chem. Commun.* **2015**, *51*, 16061–16064.

[40] Hou, H. S.; Shao, L. D.; Zhang, Y.; Zou, G. Q.; Chen, J.; Ji, X. B. Large-area carbon nanosheets doped with phosphorus: A high-performance anode material for sodium-ion batteries. *Adv. Sci.* **2017**, *4*, 1600243.

[41] Xie, K.; Qin, X. T.; Wang, X. Z.; Wang, Y. N.; Tao, H. S.; Wu, Q.; Yang, L. J.; Hu, Z. Carbon nanocages as supercapacitor electrode materials. *Adv. Mater.* **2012**, *24*, 347–352.

[42] Zhao, J.; Lai, H. W.; Lyu, Z. Y.; Jiang, Y. F.; Xie, K.; Wang, X. Z.; Wu, Q.; Yang, L. J.; Jin, Z.; Ma, Y. W. et al. Hydrophilic hierarchical nitrogen-doped carbon nanocages for ultrahigh supercapacitive performance. *Adv. Mater.* **2015**, *27*, 3541–3545.

[43] Ma, Y.; Skytt, P.; Wassdahl, N.; Glans, P.; Guo, J.; Nordgren, J. Core excitons and vibronic coupling in diamond and graphite. *Phys. Rev. Lett.* **1993**, *71*, 3725–3728.

[44] Ehlert, C.; Unger, W. E. S.; Saalfrank, P. C K-edge NEXAFS spectra of graphene with physical and chemical defects: A study based on density functional theory. *Phys. Chem. Chem. Phys.* **2014**, *16*, 14083–14095.

[45] Kaznacheyev, K.; Osanna, A.; Jacobsen, C.; Plashkevych, O.; Vahtras, O.; Ågren; Carravetta, V.; Hitchcock, A. P. Innershell absorption spectroscopy of amino acids. *J. Phys. Chem. A* **2002**, *106*, 3153–3168.

[46] Heymann, K.; Lehmann, J.; Solomon, D.; Schmidt, M. W. I.; Regier, T. C 1s K-edge near edge X-ray absorption fine structure (NEXAFS) spectroscopy for characterizing functional group chemistry of black carbon. *Org. Geochem.* **2011**, *42*, 1055–1064.

[47] Zhou, J. G.; Wang, J.; Liu, H.; Banis, M. N.; Sun, X. L.; Sham, T. K. Imaging nitrogen in individual carbon nanotubes. *J. Phys. Chem. Lett.* **2010**, *1*, 1709–1713.

[48] Gao, Y. J.; Hu, G.; Zhong, J.; Shi, Z. J.; Zhu, Y. S.; Su, D. S.; Wang, J. G.; Bao, X. H.; Ma, D. Nitrogen-doped sp^2-hybridized carbon as a superior catalyst for selective oxidation. *Angew. Chem., Int. Ed.* **2013**, *52*, 2109–2113.

[49] Pan, B. B.; Zhu, X. R.; Wu, Y. L.; Liu, T. C.; Bi, X. X.; Feng, K.; Han, N.; Zhong, J.; Lu, J.; Li, Y. F. et al. Toward highly selective electrochemical CO_2 reduction using metal-free heteroatom-doped carbon. *Adv. Sci.* **2020**, *7*, 2001002.

[50] Jiao, Y.; Zheng, Y.; Davey, K.; Qiao, S. Z. Activity origin and catalyst design principles for electrocatalytic hydrogen evolution on heteroatom-doped graphene. *Nat. Energy* **2016**, *1*, 16130.

[51] Xiong, W. H.; Peng, J.; Hu, Y. F. Use of X-ray absorption near edge structure (XANES) to identify physisorption and chemisorption of phosphate onto ferrihydrite-modified diatomite. *J. Colloid Interface Sci.* **2012**, *368*, 528–532.

[52] Zhu, X. J.; Zhang, T. M.; Jiang, D. C.; Duan, H. L.; Sun, Z. J.; Zhang, M. M.; Jin, H. C.; Guan, R. N.; Liu, Y. J.; Chen, M. Q. et al. Stabilizing black phosphorus nanosheets via edge-selective bonding of sacrificial C_{60} molecules. *Nat. Commun.* **2018**, *9*, 4177.

[53] Xue, X. Y.; Yang, H.; Yang, T.; Yuan, P. F.; Li, Q.; Mu, S. C.; Zheng, X. L.; Chi, L. F.; Zhu, J.; Li, Y. G. et al. N,P-coordinated fullerene-like carbon nanostructures with dual active centers toward highly-efficient multi-functional electrocatalysis for CO_2RR, ORR and Zn-air battery. *J. Mater. Chem. A* **2019**, *7*, 15271–15277.

[54] Kasrai, M.; Brown, J. R.; Bancroft, G. M.; Yin, Z.; Tan, K. H. Sulphur characterization in coal from X-ray absorption near edge spectroscopy. *Int. J. Coal Geol.* **1996**, *32*, 107–135.

[55] Wang, X. P.; Li, X. Y.; Ding, S. S.; Chen, Y. L.; Liu, Y.; Fang, M. W.; Xiao, G. Z.; Zhu, Y. Constructing ample active sites in nitrogen-doped carbon materials for efficient electrocatalytic carbon dioxide reduction. *Nano Energy* **2021**, *90*, 106541.

[56] Ye, L.; Ying, Y. R.; Sun, D. R.; Zhang, Z. Y.; Fei, L. F.; Wen, Z. H.; Qiao, J. L.; Huang, H. T. Highly efficient porous carbon electrocatalyst with controllable N-species content for selective CO_2 reduction. *Angew. Chem., Int. Ed.* **2020**, *59*, 3244–3251.

[57] Scudder, P. H. *Electron Flow in Organic Chemistry: A Decision-Based Guide to Organic Mechanisms*; 2nd ed. John Wiley & Sons: Hoboken, 2013; p 33.